

**Kinetic Modeling of  $^{18}\text{F}$ -(2S,4R)4-Fluoroglutamine in Mouse Models of Breast Cancer to Estimate Glutamine Pool Size as an Indicator of Tumor Glutamine Metabolism**

Varsha Viswanath<sup>1</sup>, Rong Zhou<sup>1</sup>, Hsiaoju Lee<sup>1</sup>, Shihong Li<sup>1</sup>, Abigail Cragin<sup>1</sup>, Robert K. Doot<sup>1</sup>, David A. Mankoff<sup>1</sup>, Austin R. Pantel<sup>1</sup>

<sup>1</sup> Department of Radiology, University of Pennsylvania, Philadelphia, PA

Financial support:

We acknowledge support from NIH KL2-TR001879, NIH R01-CA211337, Susan G Komen SAC130060, NIH R21-CA198563. We thank Calithera for generously providing CB-839.

Author responsible for correspondence:

Varsha Viswanath, Ph.D.  
Postdoctoral Fellow  
3620 Hamilton Walk, 150 John Morgan Building  
University of Pennsylvania  
Philadelphia, PA 19104  
(215) 898-4779  
fax: (215) 573-3880  
Varsha.Viswanath@pennmedicine.upenn.edu

Total # words: 6820

Running title: Modeling  $^{18}\text{F}$ -Gln in breast cancer

## ABSTRACT

*350/350 words*

The PET radiotracer  $^{18}\text{F}$ -(2S,4R)4-Fluoroglutamine ( $^{18}\text{F}$ -Gln) reflects glutamine transport and can be used to infer glutamine metabolism. Mouse xenograft studies have demonstrated that  $^{18}\text{F}$ -Gln uptake correlates directly with glutamine pool size and is inversely related to glutamine metabolism through the glutaminase enzyme. To provide a framework for the analysis of  $^{18}\text{F}$ -Gln-PET, we have examined  $^{18}\text{F}$ -Gln uptake kinetics in mouse models of breast cancer at baseline and after inhibition of glutaminase. We describe results of the pre-clinical analysis and computer simulations with the goal of model validation and performance assessment in anticipation of human breast cancer patient studies. **Methods:** Triple-negative breast cancer and receptor-positive xenografts were implanted in athymic mice. PET mouse imaging was performed at baseline and after treatment with a glutaminase inhibitor or a vehicle solution for a total of four mouse groups. Dynamic PET images were obtained for one hour beginning at the time of intravenous injection of  $^{18}\text{F}$ -FGln. Kinetic analysis and computer simulations were performed on a representative time-activity curves (TAC), testing 1- and 2-compartment models to describe kinetics. **Results:** Dynamic imaging for one hour captured blood and tumor TACs indicative of largely reversible uptake of  $^{18}\text{F}$ -FGln in tumors. Consistent with this observation, a two-compartment model indicated a relatively low estimate of trapping ( $k_3$ ), suggesting that the one-compartment model is preferable. Logan plot graphical analysis demonstrated late linearity, supporting reversible kinetics and modeling with a single compartment. Analysis of the mouse data and simulations suggests that estimates of glutamine pools size, specifically the  $V_D$  for  $^{18}\text{F}$ -FGln, were more reliably estimated using the one-compartment reversible model compared to the two-compartment irreversible model. Tumor-to-blood ratios, a more practical potential proxy of  $V_D$ , demonstrated good correlation with volume of distribution from single-compartment models and Logan analyses. **Conclusions:** Kinetic analysis of dynamic  $^{18}\text{F}$ -Gln-PET images demonstrated the ability to measure  $V_D$  to estimate glutamine pool size, a key indicator of cellular

glutamine metabolism, by both a one-compartment model and Logan analysis. Changes in  $V_D$  with glutaminase inhibition supports the ability to assess response to glutamine metabolism-targeted therapy. Concordance of kinetic measures with tumor-to-blood ratios provides a clinically feasible approach for human imaging.

**Keywords:** Kinetic modeling, Numerical simulations,  $^{18}\text{F}$ -Glutamine, Animal imaging, Triple negative breast cancer

## INTRODUCTION

Malignant cells reprogram pathways of energy metabolism for accelerated growth (1), providing opportunities for imaging and targeted treatment. Dysregulated glucose metabolism has been leveraged for PET imaging with <sup>18</sup>F-fluorodeoxyglucose (<sup>18</sup>F-FDG), a tracer that has shown broad clinical applicability, in clinical oncologic imaging (2). A growing body of research suggests that dysregulated cellular metabolism extends beyond that of increased glucose consumption (3). Complementary to glucose, cancers may consume glutamine, the most abundant amino acid in the plasma (4). Glutamine has numerous cellular metabolic fates. It can serve as an alternative energy substrate to glucose and as source for building carbon skeletons and for nitrogen metabolism and biosynthesis (5-8). Numerous oncogenes and tumor suppressor genes have been implicated in the control of glutamine metabolism, most notably upregulation of the MYC oncogene (7).

Oncogene-dependent reliance on glutamine is a cancer vulnerability that has been exploited for therapeutic gain. The first step in the glutaminolysis, the conversion of glutamine to glutamate via the glutaminase enzyme, represents a prime target to inhibit the entire pathway and several inhibitors have been developed (9-11). The glutaminase inhibitor CB-839 (Calithera Biosciences) has demonstrated antiproliferative activity in cell lines with accelerated glutamine metabolism, including triple-negative breast cancer (TNBC) cell lines (11,12). Sensitivity of breast cancer cell lines to CB-839 correlated with glutaminase activity and baseline glutamate:glutamine cellular concentration ratio, an indirect measure of glutaminase activity (11,12). The generally increased glutaminase activity and susceptibility of TNBC to CB-839 has supported clinical trials of this agent in patients with TNBC. In both treatment-naïve and pre-treated cohorts, partial responses were achieved in some, but not all, patients (13,14). The variable activity of CB-839 between cell lines and non-uniform radiologic response in TNBC patients suggests a need for a biomarker to predict and monitor of CB-839 efficacy. Cellular studies suggest glutamine pool

size at baseline and after CB-839 could be used as a surrogate to measure cellular glutamine metabolism (11,12), and by extension, serve as a biomarker for targeted glutaminase therapy.

The PET radiotracer  $^{18}\text{F}$ -(2S,4R)4-Fluoroglutamine ( $^{18}\text{F}$ -Gln) has been developed as an in vivo measure of tumor glutamine metabolism (15) and uptake has been seen in a variety of cancers (16-19).  $^{18}\text{F}$ -Gln utilizes the same cellular transporters as native glutamine but is minimally metabolized (12,17,20). In cell uptake studies and early animal data,  $^{18}\text{F}$ -Gln generally washes out from cells over time, suggesting reversible transport (12,20). These properties make  $^{18}\text{F}$ -Gln an ideal radiotracer for measuring glutamine pool size. Indeed,  $^{18}\text{F}$ -Gln tumor-to-blood ratios demonstrated a strong positive correlation with glutamine pool size as measured by  $^1\text{H}$  magnetic resonance spectroscopy (12). However, the optimal method for PET image analysis has not been established for this experimental radiotracer. In this paper, we model the kinetics of  $^{18}\text{F}$ -Gln observed in two breast cancer xenografts in mice, using both graphical and compartmental analyses to estimate parameters relevant to glutamine transport and cellular pool size. Based on our previously published pre-clinical data (12), we hypothesize that the distribution volume of  $^{18}\text{F}$ -Gln is a marker of tumor glutamine pool size which can be used to infer levels of tumor glutaminolysis. Based on known biology of  $^{18}\text{F}$ -Gln, a two-compartment model with a small amount of trapping should best model the data. However, we hypothesize that the rate of trapping will be difficult to estimate which in turn will affect the estimation of glutamine pool size, the kinetic parameter of interest. To quantify this, computer simulations were used to study the mathematical properties of the model, with the goal of building a foundation for quantitative interpretation of  $^{18}\text{F}$ -Gln in human studies.

## MATERIALS AND METHODS

### MOUSE MODELS

Human breast cancer xenografts were established in mice as previously described (12). Briefly, xenografts from HCC1806 (triple-negative breast cancer cell line) and MCF-7 (receptor-positive breast

cancer cell line) were implanted in NCR athymic nu/nu mice subcutaneously. The glutaminase activity in these cell lines have been shown to be high for the HCC1806 xenograft and low in the MCF-7 xenograft (11). Tumors were allowed to grow to adequate size as measured by calipers on the skin prior to each PET scan (baseline 270-1057 mm<sup>3</sup>, post-treatment 210-1374 mm<sup>3</sup>). The glutaminase inhibitor CB-839 was supplied through a generous material transfer agreement by Calithera Biosciences (South San Francisco, California, USA). CB-839 was dissolved in the vehicle solution (VEH) and administered via oral gavage (200 mg/kg twice daily). Control (VEH) mice received the same volume of vehicle solution without CB-839 added. Four to six doses of CB-839 or VEH were administered. The post-treatment scan was performed at least 4 hours after the last CB-839 administration to allow for adequate absorption. This short treatment course was given to ensure a metabolic effect of glutaminase inhibition without changes in overall tumor volume that could confound image interpretation, as documented in prior studies (12).

Six HCC1806 xenografts and 6 MCF-7 xenografts were analyzed. Each subtype includes three CB-839 treated and three VEH treated mice. Two mice were scanned at baseline, then after VEH treatment, and subsequently treated with CB-839 and scanned. The initial pre-treatment scan was used as baseline for the post-CB-839 scan.

#### **<sup>18</sup>F-GLN RADIOSYNTHESIS**

<sup>18</sup>F-Gln was synthesized as previously described (15,21). Radiochemical purity was greater than 90%. Specific activity was greater than 4,847 MBq/mol; the detection limit was less than 5 µg/mL.

#### **<sup>18</sup>F-GLN PET STUDIES**

A dedicated small animal PET scanner was utilized for all studies (A-PET), with technical parameters and performance characteristics as detailed in (22). The spatial resolution is 2.3 mm and the 3D row-action maximum likelihood algorithm (3D RAMLA) (23) was used for reconstruction into 1 mm<sup>3</sup> isotropic resolution. Images were decay corrected; scatter and attenuation correction were not used,

noting the small size of a mouse. Mice were sedated during the imaging via inhaled 1 L/min oxygen containing 1.5% isoflurane via nose cone.

All mice were scanned using the following dynamic imaging protocol. PET imaging was initiated immediately prior to a tail vein injection of 11.1-12.95 MBq (300-350  $\mu$ Ci) of  $^{18}\text{F}$ -Gln injection. The first ten min of dynamic imaging were acquired in list mode and parsed into 15 frames (6x10s , 9x60s). The remaining 50 min of PET data were collected in sinogram mode in 10x300s frames.

### **$^{18}\text{F}$ -GLN IMAGING ANALYSIS**

MIM version 6.7.10 was used to view PET images and draw volumes-of-interest (VOIs). To delineate VOIs for tumor TACs, a search area was manually drawn on the last 5-min frame to include the tumor and exclude nearby structures with high physiologic uptake (e.g. liver). The location of the peak VOI (i.e. the spherical VOI with a volume of 16 voxels where the mean counts were maximized within the search area) found in MIM was used to draw the VOI in Matlab, and TAC curves were constructed from mean values in the VOI. This method of selecting the VOI was based on PERCIST criteria (24) and adapted for mice imaging, while allowing us to exclude the photopenic centers of the tumors. Additionally, Matlab appropriately weights voxels that are only partially covered by the spherical VOI. TACs were corrected for frame duration and scaled to units of %ID/g as described in prior work by Zhou et al (12). These measures were also used to calculate tumor-to-blood ratios.

### **COMPARTMENTAL MODEL**

For compartmental modeling, a two-compartment model with irreversible trapping and a single blood input was used (Figure 1).  $K_1$  denotes the transport rate constant from blood to tissue.  $k_2$ , the reverse of  $K_1$ , represents the rate constant of reversible transport from the tissue compartment back to blood. Lastly,  $k_3$  represents the rate constant of tracer trapping, presumed to be due to the incorporation of tissue glutamine into macromolecules such as peptides. This model was based upon observations that

$^{18}\text{F}$ -Gln is transported into and out of cells similar to glutamine, but is minimally metabolized; therefore, the metabolite  $^{18}\text{F}$ -Glutamate is not included in the model, and the reversible compartment for  $^{18}\text{F}$ -Gln is considered to reflect the cellular glutamine pool size. The hypothesis underlying our model is therefore that  $^{18}\text{F}$ -Gln distribution volume in the reversible compartment ( $V_D$ ) provides an estimate of cellular glutamine concentration, which is the desired marker of glutaminase activity and inhibition. There is a possibility that a small fraction of  $^{18}\text{F}$ -Gln is incorporated into macromolecules (12), indicating the need for a second compartment in the model and the parameter  $k_3$ , to account for this minor effect. To indicate this,  $k_3$  is denoted with a dashed arrow in the model. In a two-compartment model, the  $V_D$  of the reversible compartment is  $V_D = K_1/(k_2 + k_3)$ . For a single-compartment model (i.e. setting  $k_3=0$ ), the distribution volume equation reverts to  $V_D = K_1/k_2$ .

We previously noted some prior reports of  $^{18}\text{F}$ -Gln to  $^{18}\text{F}$ -Glutamate metabolism. Gas chromatography-mass spectroscopy cellular studies report minimal metabolism of  $^{19}\text{F}$ -Glutamine was observed (17).  $^{18}\text{F}$ -Glutamate (8-9% of total activity) was seen in the supernatant of mice and rat tumor extracts on HPLC analysis at one hour (20). We note that there has been an alternative compartment model proposed for  $^{18}\text{F}$ -Gln that hypothesize significant metabolism of  $^{18}\text{F}$ -Gln to  $^{18}\text{F}$ -Glutamate (19). Our prior studies in breast cancer mouse models demonstrated that  $\geq 85\%$  of the radioactivity in the supernatant of tumor tissue was in the form of  $^{18}\text{F}$ -Gln and only 9-14% of activity was from metabolites (12). Much of  $^{18}\text{F}$ -Glutamate may be related to blood metabolites that arise from degradative organs such as liver and kidney, as 82% - 87% of blood radioactivity was in the form  $^{18}\text{F}$ -Gln and less than 16% was from metabolites (12). We therefore consider alternative models that include the possibility of tumor tissue metabolism to  $^{18}\text{F}$ -Glutamate as well as the transport of  $^{18}\text{F}$ -Glutamate as a blood metabolite to tissue (Supplemental Figure 1). However, since metabolism of  $^{18}\text{F}$ -Gln to  $^{18}\text{F}$ -Glutamate appears to be minimal in most reported studies, we focus our analysis largely on the model illustrated in Figure 1.



## KINETIC PARAMETER ESTIMATION

Tumor and blood TACs derived above were input into PMOD Version 3.7 (Pmod Technologies, LLC, Zurich, Switzerland). Image-derived arterial input functions served as the input to the model for all analyses, and raw data obtained from image analysis were fit empirically to a linear function until the peak of the input curve and a fitted sum of three exponentials after the peak as implemented in PMOD to reduce input noise, as has been performed in a number of other similar studies (25). For compartmental analysis, model parameters were estimated using the Levenberg- Marquardt least-squares minimization algorithm as implemented in PMOD. Graphical analysis of blood and tumor TACs was performed using Patlak and Logan analyses (26,27), also as implemented in PMOD. For Logan plot analysis,  $V_D$  was estimated as the slope of the line of  $\int C_{plasma} dt / C_{tissue}$  versus  $\int C_{tissue} dt / C_{tissue}$ .

## MODEL CHARACTERIZATION - SENSITIVITY FUNCTION

To test the mathematical behavior of the model, idealized uptake curves based on representative TNBC and ER+ mouse, each treated with CB-839, were selected as a basis for further analysis. Akaike Information Criteria (AIC) as calculated by PMOD was used to compare compartmental models (28). To characterize the kinetic models and performance in parameter estimation, sensitivity functions were calculated for each parameter using PMOD. In addition, the parameter identifiability matrices were estimated to determine the ability to independently estimate parameters ( $K_1$ ,  $K_1/k_2$ , and  $k_3$ ) for the model (29).

## PARAMETER ESTIMATION PERFORMANCE ASSESSMENT USING SIMULATED CURVES WITH ADDED POISSON NOISE

To measure the precision and bias of estimated parameters, TACs from each of the two representative mice were fit using a 1-compartment, reversible 2-compartment, and irreversible 2-compartment model in PMOD. Radioactive delay, frame duration, and decay were applied to the TACs to calculate counts collected in the tumor, and Poisson noise was added to each datapoint to generate 1000

noise realizations ( $\lambda = \text{counts}$ ,  $\sigma = \sqrt{\lambda}$ ). These curves were fit in PMOD using the corresponding compartmental model to assess robustness of kinetic parameter estimation.

We then extended the simulation to use measured kinetic parameters from all imaged mice. Parameters were input into STELLA, a model integration program (Stella 1.9.1, ISEE systems, Lebanon, NH), to generate 250 TACs for a 1-compartment model and an irreversible 2-compartment model. Poisson noise was added to these curves, as described above, to generate 100 noise realizations per curve, and all TACs were fit in PMOD. Finally, to determine the effect of ignoring  $k_3$  on  $V_D$  estimation, idealized curves from Stella were used to model a two-compartment model with variable levels of trapping.

#### **STATISTICAL ANALYSIS**

Pearson correlation coefficients were calculated for pairwise comparisons between  $V_D$  estimates for each model.  $R^2$  values were calculated to evaluate the fit of graphical analyses and correlation between  $V_D$  for different models and tumor-to-blood ratios .

#### **RESULTS**

##### **BLOOD AND TISSUE TIME ACTIVITY CURVES**

Representative blood and tissue TACs are shown in Figure 2, along with the final frame imaged. At baseline, TNBC xenografts with inherently high glutaminase activity demonstrate low  $^{18}\text{F}$ -Gln uptake compared to an ER+ xenograft with inherently low glutaminase activity (Figure 2). Upon glutaminase inhibition with CB-839, there is increased radiotracer uptake in the TNBC tumor reflecting an increase in glutamine pool size which is expected with the inhibition of glutaminolysis. In the ER+ tumor xenograft, only a minimal increase in radiotracer uptake was observed after glutaminase inhibition, reflecting known low glutaminase activity in this breast cancer subtype.

## COMPARTMENTAL ANALYSIS OF XENOGRAFT DATA

The two representative mice with typical TACs shown above in Figure 2 were then selected for mathematical investigation of radiotracer uptake. Both a single-compartment and a two-compartment model with trapping were investigated. The one-compartment fit is shown in Figure 3A,C and the two-compartment fit is shown Figure 3B,D. The blood fraction was fixed at 5% for these models and not estimated. A blood fraction of 5% is within the range of estimated values from a prior mouse xenograft studies (30) and similar to the 4% blood fraction used in prior studies of  $^{18}\text{F}$ -FDG in locally advanced breast cancer in humans (31).

The single-compartment model for the ER+ tumor underestimates  $^{18}\text{F}$ -Gln uptake at later time points, unlike the 2-compartment model that includes the possibility of retained tracer in a non-reversible compartment. The two-compartment model estimates  $k_3$  at 0/min for the TNBC mouse and 0.006/min for the ER+ mouse data, where 27% of the total radioactivity is estimated to be contained in the nonreversible compartment at 60-min. This estimate is higher than the  $10\% \pm 4\%$  of radiotracer incorporated into the pellet versus supernatant of tumor extracts in prior work (12), perhaps owing to the difficulty of estimating a small  $k_3$ , as supported by simulation data below. This finding, and the relatively low values of  $k_3$  found across all animals studied suggest that such a term could be omitted.

The Akaike information criterion (AIC) of the TNBC mouse data fit using a single-compartment model was 60.9, more favorable than the AIC of a two-compartment model of 63.5; the penalty of fitting an extra term in the two-compartment model more than offset the slightly improved goodness-of-fit by the two-compartment model. The AIC for the ER+ tumor data fit using a single- and two-compartment model were nearly equal: 34.4 and 33.8, respectively, noting the discrepancy between  $k_3$  estimates for the 2-compartment model for ER+ tumors and measured data, described above. The benefits of omitting

the second compartment are further supported by examining the accuracy and precision estimates of estimating  $k_3$  as described below.

#### **GRAPHICAL ANALYSIS OF XENOGRAFT DATA**

Analysis using Patlak and Logan graphical approaches are shown in Figure 4. The Logan plots (Figure 4A,C) demonstrated late linearity, consistent with minimal radiotracer trapping and largely reversible tracer exchange between the tumor and the blood.  $R^2$  values for the fits of the TNBC and ER+ mice data were 0.997 and 0.999, respectively, reflecting good quality linear fits. In contrast, the Patlak plot demonstrates poor fits, arguing against irreversible radiotracer trapping,  $R^2$  of 0.91 and 0.83 for the TNBC and ER+ mice data, respectively, were obtained using fewer data points than the Logan fit. Graphical analyses support the use of the  $V_D$  as calculated by the slope of the best fit line in the Logan graphical analysis as a measure of glutamine pool size. The applicability of Logan analysis is consistent with the suitable fits of the single-compartment model.

#### **MODEL CHARACTERIZATION SENSITIVITY AND IDENTIFIABILITY ANALYSIS**

The sensitivity function for the two mice fit using an irreversible two-compartment model (Supplemental Figure 2) suggest that both models are most sensitive to  $K_1$  early after injection, more sensitive to  $K_1/k_2$  at intermediate time points, and most sensitive to  $k_3$  at late time points. The identifiability matrix (Supplemental Table I) for the 2-compartment model suggests that  $K_1$  and  $K_1/k_2$  can be estimated independently, but that  $K_1/k_2$  and  $k_3$  has a high covariance (-0.97) and cannot be estimated independently, suggesting that errors in  $k_3$  estimation will propagate into  $V_D$  and supports the exclusion of  $k_3$  in the model.

#### **EFFECT OF GLUTAMINASE THERAPY ON VOLUME OF DISTRIBUTION AND TUMOR-TO-BLOOD RATIOS**

After glutaminase inhibition,  $V_D$  increased in TNBC xenografts, but not consistently in MCF-7 xenografts nor VEH-treated TNBC tumors (Figure 5). Of the four TNBC tumors treated with CB-839, three

had an increase in  $V_D$  (18%, 42%, and 89%), while one had a decrease after treatment. This study was not powered to detect increase in  $V_D$  after glutaminase inhibition in any subgroup. One of the four mice had a markedly elevated  $V_D$  at baseline above the others, indicative of less glutaminolysis and atypical of TNBC. Previously, we showed a 4.3-fold increase in glutamine pool size by MRS in TNBC xenografts after glutaminase inhibition. Given a 2.5-fold increase in plasma glutamine concentration with glutaminase inhibition, an increase in tumor-to-blood ratio and  $V_D$  of  $4.3/2.5=1.7$  would be expected (12). Additionally, variability in PET signal response to CB-839 supports differential glutaminase inhibition in breast cancer subtypes and supports the need for a biomarker to measure glutamine metabolism.

#### **SIMULATION OF PARAMETERS ESTIMATION**

Simulations (Figure 6A) revealed that the precision and accuracy in recovering the true  $V_D$  was better for the one-compartment model than either two-compartment model. The reversible two-compartment model (Supplemental Figure 1B) cannot accurately or precisely estimate  $V_D$  and was not further studied. The average bias of the median  $V_D$  and the %SD of the IQR (supplemental equation I) are markedly improved for the one-compartment model compared to the irreversible two-compartment model (Bias: <0.5% vs 1.6-12.9%; %SD: 7.73-20.2% vs 19.4-54.3%), demonstrating the robustness of the one-compartment model in contrast to the poor performance of the 2-compartment model.

Simulations which used kinetic parameters from all mice (Figure 6B) clearly demonstrate more precise recovery of the true  $V_D$  when estimated using a one-compartment model, in agreement with simulations in Figure 6A. The average %SD, calculated as  $\%SD = stdev/mean$  for each data point, is  $12\% \pm 4.2\%$  for the one-compartment model and  $33\% \pm 30\%$  for the two-compartment model with trapping.

The accuracy and precision of the individual recovered kinetic parameters ( $K_1$  and  $k_3$ ) in the simulations described above are shown in Supplemental Figure 3.  $K_1$  was better estimated using the one-

compartment model.  $k_3$  estimation with an irreversible two-compartment model has a large bias and %SD, resulting in overestimation of activity in the trapped compartment (Figure 3D). Additionally, errors in  $k_3$  propagate to errors in  $V_D$ .

#### COMPARISON OF $V_D$ AND TUMOR-TO-BLOOD RATIOS

For all imaged mice,  $V_D$  estimates were compared with tumor-to-blood ratios (Figure 7), which serve as a proxy of  $V_D$  obtained from static images, using the final time-point. Strong correlations were seen between tumor-to-blood ratios versus  $V_D$  estimated by Logan plot or a single-compartment model, but not a two-compartment model. This underscores the inaccuracy of using a two-compartment model to estimate  $V_D$ , and thus glutamine pool size.

#### ALTERNATIVE COMPARTMENTAL MODELS

We considered alternative compartmental models (Supplemental Figure 1B and 1C) that included the possibility of reversible  $^{18}\text{F}$ -Gln metabolism to  $^{18}\text{F}$ -Glutamate in tumor tissue. These models, specifically model 1B, were able to fit the data well, but near 50% of fits resulted in a near-zero  $k_4$  or  $k_3$  value, or a  $k_4$  value so large ( $\sim 8 \text{ min}^{-1}$ ) that the ratio of  $k_3/k_4$ , the  $V_D$  of  $^{18}\text{F}$ -Glutamate, is essentially zero. The other half of fits resulted in rates of washout from the reversible compartment ( $k_4$  or  $k_4+k_5$ ) that were comparable in magnitude to the  $k_3$  metabolism rate (i.e.  $k_3/k_4 = 1.06 \pm 1.08$ ). This implies a small distribution volume for  $^{18}\text{F}$ -Glutamate comparable to  $^{18}\text{F}$ -Gln; however, in the glutaminolytic TNBC cells,  $^{18}\text{F}$ -Glutamate would be retained in a large intracellular pool of glutamate in cells actively metabolizing glutamine to glutamate (11,32). Liquid chromatography-tandem mass spectrometry studies (LC/MS-MS) on HCC-1806 TNBC tumors demonstrates a tumor glutamate concentration approximately 5 times greater than tumor glutamine concentration (11), implying that the  $V_D$  of glutamate (i.e.  $k_3/k_4$ ) should be 5x the  $V_D$  of glutamine (5-10 ml/cm<sup>3</sup>, given a  $V_D$  of glutamine 1-2 ml/cm<sup>3</sup>). Thus, models that include finite tumor

metabolism of  $^{18}\text{F}$ -Gln to  $^{18}\text{F}$ -Glutamate do not appear to fit the observed tracer kinetic data in the mouse models and the known high concentration of glutamate in glutaminolytic cells.

We also tested a model that included transport of  $^{18}\text{F}$ -Glutamate, as a labeled metabolite in the blood, to tumor tissue (Supplemental Figure 1D). To explore this, we divided the arterial input curve into principal components of  $^{18}\text{F}$ -Gln and  $^{18}\text{F}$ -Glu based on sampled blood data (12). We estimated  $K_1'$  and  $k_2'$  (glutamate kinetic parameters) at 10% of their respective glutamine counterparts ( $K_1$  and  $k_2$ ). As shown in Supplemental Figure 4, the contribution of PET signal from tissue  $^{18}\text{F}$ -Glu is largely linear over time and accounts for a small component of the total PET signal at later time points. This small  $^{18}\text{F}$ -Glu component (8%) could account for underestimates of the model curve of a single-compartment model at later time points. The relatively small contribution of glutamate suggests that it can likely be ignored, particularly at earlier time points.

## DISCUSSION

Our study provides a theoretical framework for kinetic analysis of  $^{18}\text{F}$ -(2S,4R)4-Fluoroglutamine ( $^{18}\text{F}$ -Gln) in mouse xenografts of human breast cancer. Previous work showed a linear relationship between  $^{18}\text{F}$ -Gln tumor-to-blood ratios and tumor glutamine concentration, and demonstrated an increase in glutamine pool size after targeted glutaminase inhibition of TNBC mice, but not ER+ mice (12). Based on radiotracer biology, a two-compartment irreversible model should fit the data well; however, the small value of  $k_3$  is difficult to estimate accurately and leads to spurious estimates of  $V_D$  of  $^{18}\text{F}$ -Gln. Thus, a one-compartment model is favored, and correlates well with changes in glutamine pool size after glutaminase inhibition. The distinctive kinetics of  $^{18}\text{F}$ -Gln necessitate specific model and image analysis approaches distinct from those used for other cancer tracers such as  $^{18}\text{F}$ -FDG (33) and this paper establishes a new imaging paradigm for this novel radiotracer which is now being used in several clinical trials.

We first demonstrated that dynamic TACs and the images recapitulated the previously described patterns of uptake (12). That is,  $^{18}\text{F}$ -Gln uptake late after injection was lower in TNBC versus ER+ models, inversely related to glutaminase activity in those cell lines (11).  $^{18}\text{F}$ -Gln uptake increased in the highly glutaminolytic tumor (TNBC) after glutaminase inhibition, but not in the low glutaminase ER+ lines (12). This was accurately captured by the  $^{18}\text{F}$ -Gln distribution volume,  $V_D$ , which estimates the cellular glutamine pool size, supporting the utility of this measure as a pharmacodynamic measure of *glutaminase* inhibitor therapy.

Based on the biochemistry of glutamine and the imaging analog,  $^{18}\text{F}$ -Gln, a one-compartment reversible model and a two-compartment irreversible model were investigated in two representative mice. The second compartment in the 2-compartment model represents incorporation of  $^{18}\text{F}$ -Gln into macromolecules, likely peptides. The two-compartment model overestimated the percentage of radiotracer incorporated into macromolecules in an ER+ mouse compared with data from prior tumor extract studies (12) suggesting error in estimating  $k_3$ . The TNBC model, with inherently high glutaminase expression, had negligible trapping. Sensitivity analysis of the two-tissue compartmental model with irreversible trapping demonstrated relative insensitivity of the model to  $k_3$ , other than late after injection, suggesting that this parameter could not be estimated accurately (Supplemental Figure 2). Simulations provided additional support for omitting  $k_3$  from the final model. Graphical analysis supported the use of a reversible model, in this case the single-compartment model. Thus, analysis of xenograft model data, model performance characteristics, and model simulations support the use of a one-compartment model to estimate the key  $^{18}\text{F}$ -Gln parameter,  $V_D$ .

The strong correlation between tumor-to-blood ratios and  $V_D$  of a single-compartment model and slope of a Logan plot (Figure 7) suggests static protocols could be considered for human imaging and should be a focus of early human studies. However, ignoring tracer trapping in the one-compartment



model could bias  $V_D$  estimation for modest levels of trapping, as shown in simulation without added noise (Supplemental Figure 5). This can be mitigated by imaging at earlier time points (e.g. 20-30 min) which should be examined in human imaging studies.

Our proposed model and results are consistent with other pre-clinical and early clinical studies. Schulte et al. showed that the pharmacologic inhibition of glutamine transport in a TNBC mouse model resulted in reduced early uptake and decreased late retention with kinetics consistent with our one-compartment model (34).  $^{18}\text{F}$ -Gln-PET has been explored as a measure of glutamine metabolism in early clinical trials.  $^{18}\text{F}$ -Gln uptake was seen in a variety of cancers: paraganglioma, breast, colon, lung, pancreas, neuroendocrine, glioma, and thyroid (16-19,35). Down sloping TACs in these human tumors support reversible kinetics. Preliminary analysis of a patient from this trial demonstrates plausibility of a one-compartment model based on good agreement of  $V_D$  between the Logan fit and the one-compartment fit (Supplemental Figure 6). The application of the framework established here in mouse xenografts can be applied to human  $^{18}\text{F}$ -Gln imaging. Although the biology in human tumors may vary from the mice xenografts and warrant use of a slightly altered kinetic model, the methodologies developed in this paper will permit the testing of these hypotheses (16). Further analysis of human studies is warranted.

We examined alternative compartment models that included the possibility of tumor metabolism of  $^{18}\text{F}$ -Gln to  $^{18}\text{F}$ -Glutamate suggested by others (19), based upon observation of defluorination of  $^{18}\text{F}$ -Gln in human studies (16) and some enzymatic studies demonstrating metabolism of  $^{18}\text{F}$ -Gln to  $^{18}\text{F}$ -Glutamate (36). While these models are able to fit our mouse data, the estimated parameters grossly underestimated the size of the tumor glutamate pool, as measured in prior studies, including our studies in TNBC mouse models (11,12). It is possible that kinetics differs in humans, although our early human data show a good fit for our one-compartment model (Supplemental Figure 6). We also examined the small impact of labeled metabolites, which may explain the inability of the one-compartment model to fit the later portion

of some observed curves. This appears to have a small impact on the estimate of  $^{18}\text{F}\text{-Gln } V_D$  but should be studied carefully in human data.

There are several limitations to the broad application of this small animal imaging study. Although two cell lines were used in this study, we believe these results are generalizable to other cell lines given the mechanism of uptake and lack of metabolism of the radiotracer. Subcutaneously implanted tumors may have different intrinsic biologic properties than human breast tumors, precluding direct translation. For example, cellularity is not a factor in mice xenografts, but may complicate the interpretation of  $V_D$  in humans, possibly necessitating a normalization factor. Future studies using other cell lines (especially TNBC), mouse models, and human imaging should address these limitations.

VOI analysis of mouse image varies greatly across studies, but our method which was based on the PERCIST criteria was designed to reproducibly draw a spherical VOI over the tumor. Our method ensured that the search area did not erroneously cover the mouse liver or knee, and the photopenic center of the tumor would not be included in the VOI. TACs were then scaled to %ID/g using the total counts in the final image, as opposed to the total injected dose. Although this is not standard, it does not affect our results since both the blood and tumor TACs are image-derived and thus similarly scaled for kinetic analysis. Additionally, we fit the image-derived blood TAC to a tri-exponential to reduce noise, as is typically common for human imaging, as opposed to direct blood sampling of the mouse. The image-derived blood curve is more representative of human imaging and better represents estimation of  $V_D$  in human trials.

Mouse imaging estimates of TACs are less accurate than human TACs owing, in part, to differences in uptake, especially for estimates of the blood input function. An image-derived blood input function was used without metabolite correction. Minimal metabolism of  $^{18}\text{F}\text{-Gln}$  in the blood supports such an input function (12), though others have used corrected input functions (19,37). Peripheral metabolism of  $^{18}\text{F}$ -

Gln to  $^{18}\text{F}$ -Glutamate may further confound the interpretation of  $^{18}\text{F}$ -Gln uptake in tumors, but as noted, the effect appears to be small and may be able to be ignored, particularly at earlier time points. Finally, our modeling work is specific to  $^{18}\text{F}$ -Gln and cannot be applied to  $^{11}\text{C}$ -Gln which has a much more complex kinetic modeled and is under preliminary investigation (38).

Our compartment model assumed no tumor metabolism of  $^{18}\text{F}$ -Gln to  $^{18}\text{F}$ -Glutamate, based upon our prior mouse model studies (12). However, based the observation of defluorination of  $^{18}\text{F}$ -Gln in human studies (16) and some enzymatic studies demonstrating metabolism of  $^{18}\text{F}$ -Gln to  $^{18}\text{F}$ -Glutamate (36), other groups have hypothesized that there might be tumor metabolism of  $^{18}\text{F}$ -Gln by glutaminase and proposed a two-compartment reversible model (Supplemental Figure 1B) (19). However, parameter estimates obtained from the model with two reversible compartments were not compatible with the large glutamate pool size observed in glutaminolytic tumors by a variety of methods (11,12,32). Rapid metabolism of  $^{18}\text{F}$ -Glutamate by alanine aminotransferase with resultant defluorination and efflux of the label from the tumor cell (Supplemental Figure 1C) (19,36) also yield estimates of glutamate pool size that are much smaller than reported and therefore thought to be a less likely explanation for the observed kinetics.

## CONCLUSION

This work found  $^{18}\text{F}$ -Gln uptake in breast xenograft models to be largely reversible, consistent with the hypothesis that  $^{18}\text{F}$ -Gln exchanges with the intracellular glutamine pool. Using a combination of traditional modeling and simulations, we determined that a one-compartment model best estimated  $V_D$  and robust estimates of  $V_D$  can also be found using Logan graphical analysis or tumor-to-blood ratios at 60-min post-injection. This study establishes a theoretical framework for analyzing further human  $^{18}\text{F}$ -Gln-PET imaging studies which have recently begun. The pairing of  $^{18}\text{F}$ -Gln with a glutaminase inhibitors to

select and monitor oncologic patients represents a prime opportunity to use molecular imaging to guide metabolically targeted cancer therapy.

#### FINANCIAL DISCLOSURES

Work presented here is partially supported by the following grants: NIH KL2-TR001879, NIH R01-CA211337, Susan G Komen SAC130060, NIH R21-CA198563. We thank Calithera for generously providing CB-839. No potential conflicts of interest relevant to this article exist.

#### ACKNOWLEDGEMENTS

We thank Eric Blankmeyer for assisting with animal imaging and Tiffany Rodriguez for analysis of the human imaging study.

#### KEY POINTS

**Question:** What kinetic model best estimates the uptake of  $^{18}\text{F}$ -Gln dynamic data and captures relevant biology?

**Pertinent Findings:** A one-compartment model accurately and precisely estimates the  $V_D$  of  $^{18}\text{F}$ -Gln, a proxy for glutamine pool size. Other models were less robust and did not reflect known glutamine biology.

**Implications for Patient Care:** The  $V_D$  from a one-compartment model captures relevant glutamine biology and will be studied in ongoing clinical studies of  $^{18}\text{F}$ -Gln in human breast cancer patient studies.

## REFERENCES

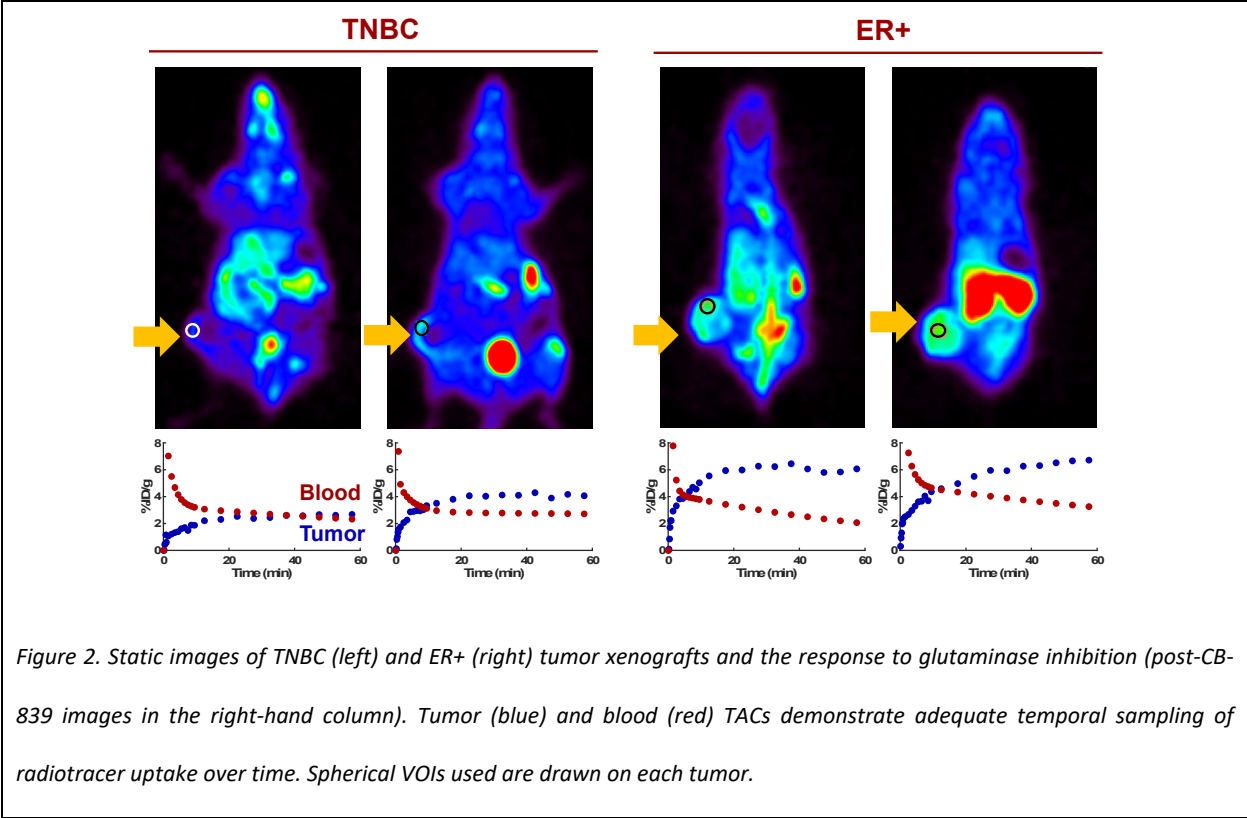
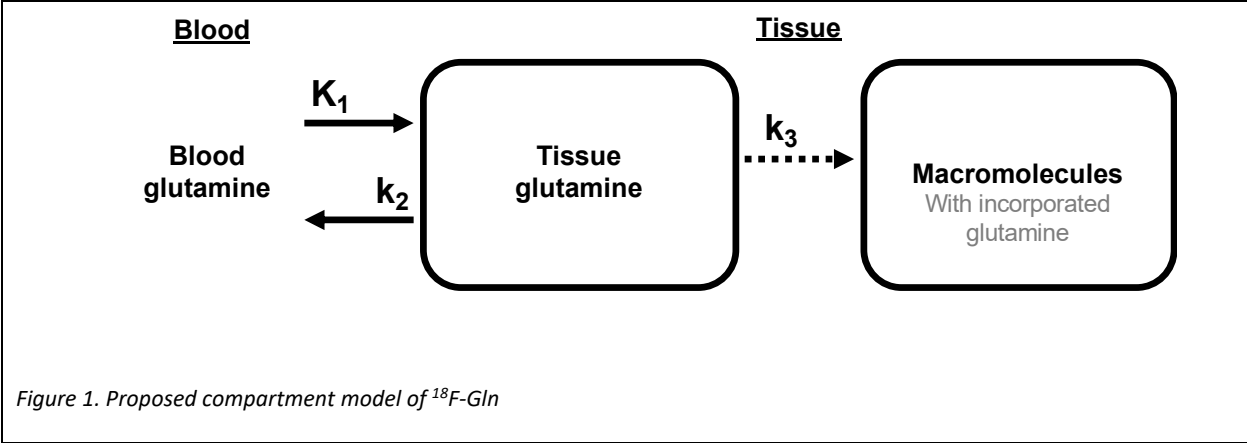
1. Hanahan D, Weinberg RA. Hallmarks of cancer: the next generation. *Cell*. 2011;144:646-674.
2. Jacques L, Jensen T, Rollins J, Caplan S, Roche J. Decision memo for positron emission tomography (FDG) for solid tumors (CAG-00181R4). *Services CfMAM*. 2013.
3. Pantel AR, Ackerman D, Lee S-C, Mankoff DA, Gade TP. Imaging cancer metabolism: underlying biology and emerging strategies. *J Nucl Med*. 2018;59:1340-1349.
4. DeBerardinis RJ, Cheng T. Q's next: the diverse functions of glutamine in metabolism, cell biology and cancer. *Oncogene*. 2010;29:313-324.
5. Hensley CT, Wasti AT, DeBerardinis RJ. Glutamine and cancer: cell biology, physiology, and clinical opportunities. *J Clin Invest*. 2013;123:3678-3684.
6. DeBerardinis RJ, Lum JJ, Hatzivassiliou G, Thompson CB. The biology of cancer: metabolic reprogramming fuels cell growth and proliferation. *Cell Metab*. 2008;7:11-20.
7. Altman BJ, Stine ZE, Dang CV. From Krebs to clinic: glutamine metabolism to cancer therapy. *Nat Rev Cancer*. 2016;16:619-634.
8. Wise DR, Thompson CB. Glutamine addiction: a new therapeutic target in cancer. *Trends Biochem Sci*. 2010;35:427-433.
9. Robinson MM, McBryant SJ, Tsukamoto T, et al. Novel mechanism of inhibition of rat kidney-type glutaminase by bis-2-(5-phenylacetamido-1,2,4-thiadiazol-2-yl)ethyl sulfide (BPTES). *Biochem J*. 2007;406:407-414.
10. Wang JB, Erickson JW, Fuji R, et al. Targeting mitochondrial glutaminase activity inhibits oncogenic transformation. *Cancer Cell*. 2010;18:207-219.
11. Gross MI, Demo SD, Dennison JB, et al. Antitumor activity of the glutaminase inhibitor CB-839 in triple-negative breast cancer. *Mol Cancer Ther*. 2014;13:890-901.
12. Zhou R, Pantel AR, Li S, et al. [18F](2S, 4R) 4-fluoroglutamine PET detects glutamine pool size changes in triple-negative breast cancer in response to glutaminase inhibition. *Cancer Res*. 2017;77:1476-1484.

13. Vidula N, Bardia A. Targeted therapy for metastatic triple negative breast cancer: The next frontier in precision oncology. *Oncotarget*. 2017;8:106167-106168.
14. Vidal G, Kalinsky K, Stringer-Reasor E, et al. Efficacy and safety of CB-839, a small molecule inhibitor of glutaminase, in combination with paclitaxel in patients with advanced triple negative breast cancer (TNBC): Initial findings from a multicenter, open-label phase 2 study. In: *Conference Record of the Cancer Research: AMER ASSOC CANCER RESEARCH 615 CHESTNUT ST, 17TH FLOOR, PHILADELPHIA, PA ...*; 2019.
15. Qu W, Zha Z, Ploessl K, et al. Synthesis of optically pure 4-fluoro-glutamines as potential metabolic imaging agents for tumors. *Journal of the American Chemical Society*. 2010;133:1122-1133.
16. Dunphy MP, Harding JJ, Venneti S, et al. In vivo PET assay of tumor glutamine flux and metabolism: in-human trial of 18F-(2S, 4R)-4-fluoroglutamine. *Radiology*. 2018;287:667-675.
17. Venneti S, Dunphy MP, Zhang H, et al. Glutamine-based PET imaging facilitates enhanced metabolic evaluation of gliomas in vivo. *Sci Transl Med*. 2015;7:274ra217.
18. Xu X, Zhu H, Liu F, et al. Dynamic PET/CT imaging of (18)F-(2S, 4R)-4-fluoroglutamine in healthy volunteers and oncological patients. *Eur J Nucl Med Mol Imaging*. 2020;47:2280-2292.
19. Grkovski M, Goel R, Krebs S, et al. Pharmacokinetic assessment of 18F-(2S, 4R)-4-fluoroglutamine in patients with cancer. *Journal of Nuclear Medicine*. 2020;61:357-366.
20. Lieberman BP, Ploessl K, Wang L, et al. PET imaging of glutaminolysis in tumors by 18F-(2S, 4R)-4-fluoroglutamine. *J Nucl Med*. 2011;52:1947-1955.
21. Li S, Schmitz A, Lee H, Mach RH. Automation of the radiosynthesis of six different (18)F-labeled radiotracers on the AllinOne. *EJNMMI Radiopharm Chem*. 2017;1:15.
22. Surti S, Karp JS, Perkins AE, et al. Imaging performance of A-PET: a small animal PET camera. *IEEE Trans Med Imaging*. 2005;24:844-852.
23. Daube-Witherspoon M, Matej S, Karp J, Lewitt R. Application of the row action maximum likelihood algorithm with spherical basis functions to clinical PET imaging. *IEEE Trans Nucl Sci*. 2001;48:24-30.
24. Wahl RL, Jacene H, Kasamon Y, Lodge MA. From RECIST to PERCIST: evolving considerations for PET response criteria in solid tumors. *J Nucl Med*. 2009;50:1225-1505.

25. Vriens D, de Geus-Oei L-F, Oyen WJ, Visser EP. A curve-fitting approach to estimate the arterial plasma input function for the assessment of glucose metabolic rate and response to treatment. *J Nucl Med*. 2009;50:1933-1939.
26. Logan J, Fowler JS, Volkow ND, et al. Graphical analysis of reversible radioligand binding from time—activity measurements applied to [N-11C-methyl]-(-)-cocaine PET studies in human subjects. *J Cereb Blood Flow Metab*. 1990;10:740-747.
27. Patlak CS, Blasberg RG. Graphical evaluation of blood-to-brain transfer constants from multiple-time uptake data. Generalizations. *J Cereb Blood Flow Metab*. 1985;5:584-590.
28. Akaike H. A new look at the statistical model identification. *IEEE Trans Automat Contr*. 1974;19:716-723.
29. Mankoff D, Muzi M, Zaidiy H. Quantitative analysis in nuclear oncologic imaging. *Quantitative analysis in nuclear medicine imaging*: Springer; 2006:494-536.
30. Kim SJ, Lee JS, Im KC, et al. Kinetic modeling of 3'-deoxy-3'-18F-fluorothymidine for quantitative cell proliferation imaging in subcutaneous tumor models in mice. *J Nucl Med*. 2008;49:2057-2066.
31. Tseng J, Dunnwald LK, Schubert EK, et al. 18F-FDG kinetics in locally advanced breast cancer: correlation with tumor blood flow and changes in response to neoadjuvant chemotherapy. *J Nucl Med*. 2004;45:1829-1837.
32. Zhou R, Bagga P, Nath K, Hariharan H, Mankoff DA, Reddy R. Glutamate-weighted chemical exchange saturation transfer magnetic resonance imaging detects glutaminase inhibition in a mouse model of triple-negative breast cancer. *Cancer Res*. 2018;78:5521-5526.
33. Mankoff DA, Farwell MD, Clark AS, Pryma DA. Making molecular imaging a clinical tool for precision oncology: a review. *JAMA Oncol*. 2017;3:695-701.
34. Schulte ML, Fu A, Zhao P, et al. Pharmacological blockade of ASCT2-dependent glutamine transport leads to antitumor efficacy in preclinical models. *Nat Med*. 2018;24:194-202.
35. Xu X, Zhu H, Liu F, et al. Dynamic PET/CT imaging of (18)F-(2S, 4R)4-fluoroglutamine in healthy volunteers and oncological patients. *Eur J Nucl Med Mol Imaging*. 2020.

- 36.** Cooper AJ, Krasnikov BF, Pinto JT, Kung HF, Li J, Ploessl K. Comparative enzymology of (2S,4R)4-fluoroglutamine and (2S,4R)4-fluoroglutamate. *Comp Biochem Physiol B Biochem Mol Biol.* 2012;163:108-120.
- 37.** Miner MW, Liljenback H, Virta J, et al. (2S, 4R)-4-[(18)F]Fluoroglutamine for In vivo PET Imaging of Glioma Xenografts in Mice: an Evaluation of Multiple Pharmacokinetic Models. *Mol Imaging Biol.* 2020.
- 38.** Padakanti P, Pantel AR, Choi H, et al. Refined analysis of [11C]L-glutamine metabolism in triple negative breast cancer xenograft model. In: *Conference Record of the World Molecular Imaging Conference.* Virtual: 2020.





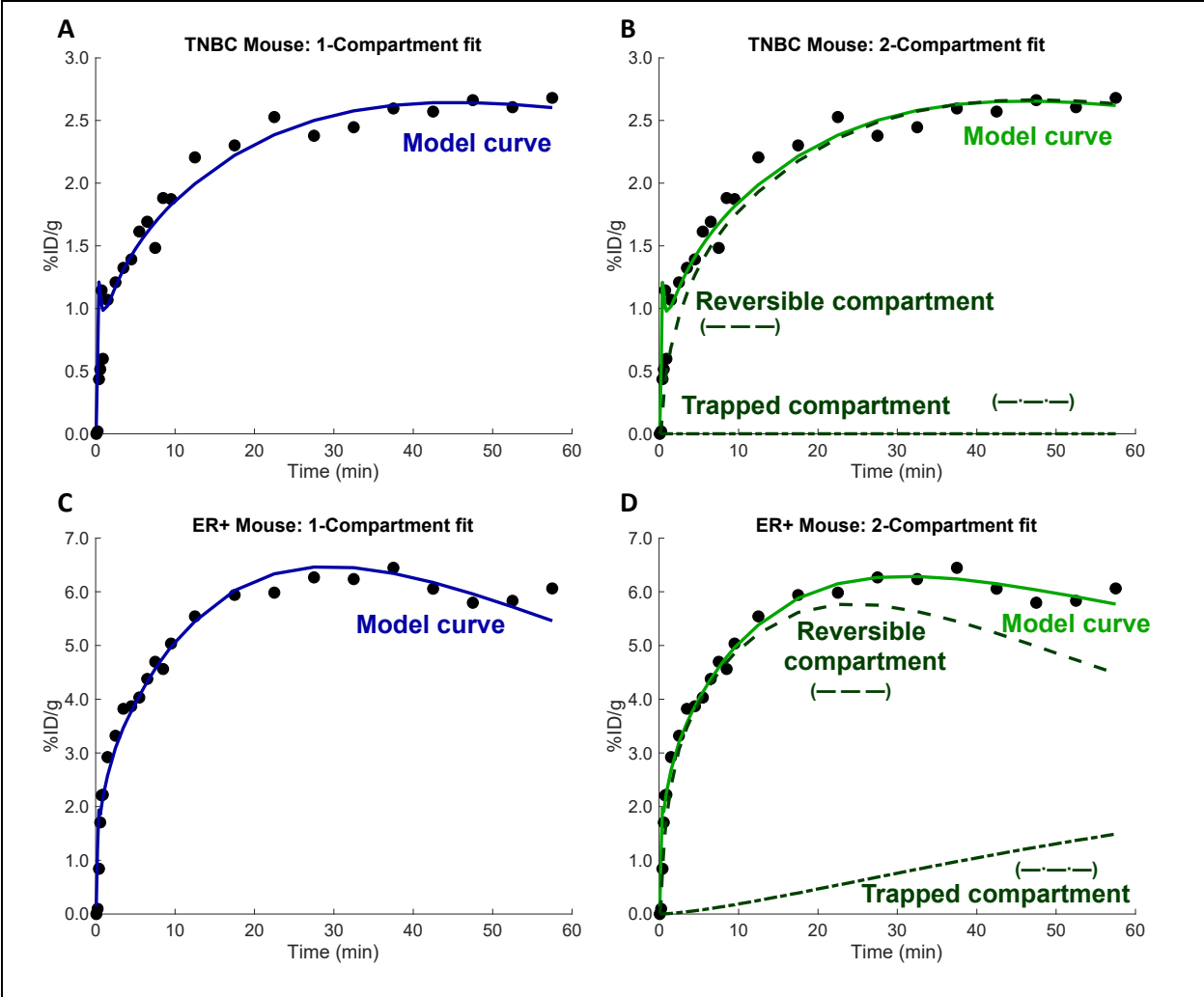
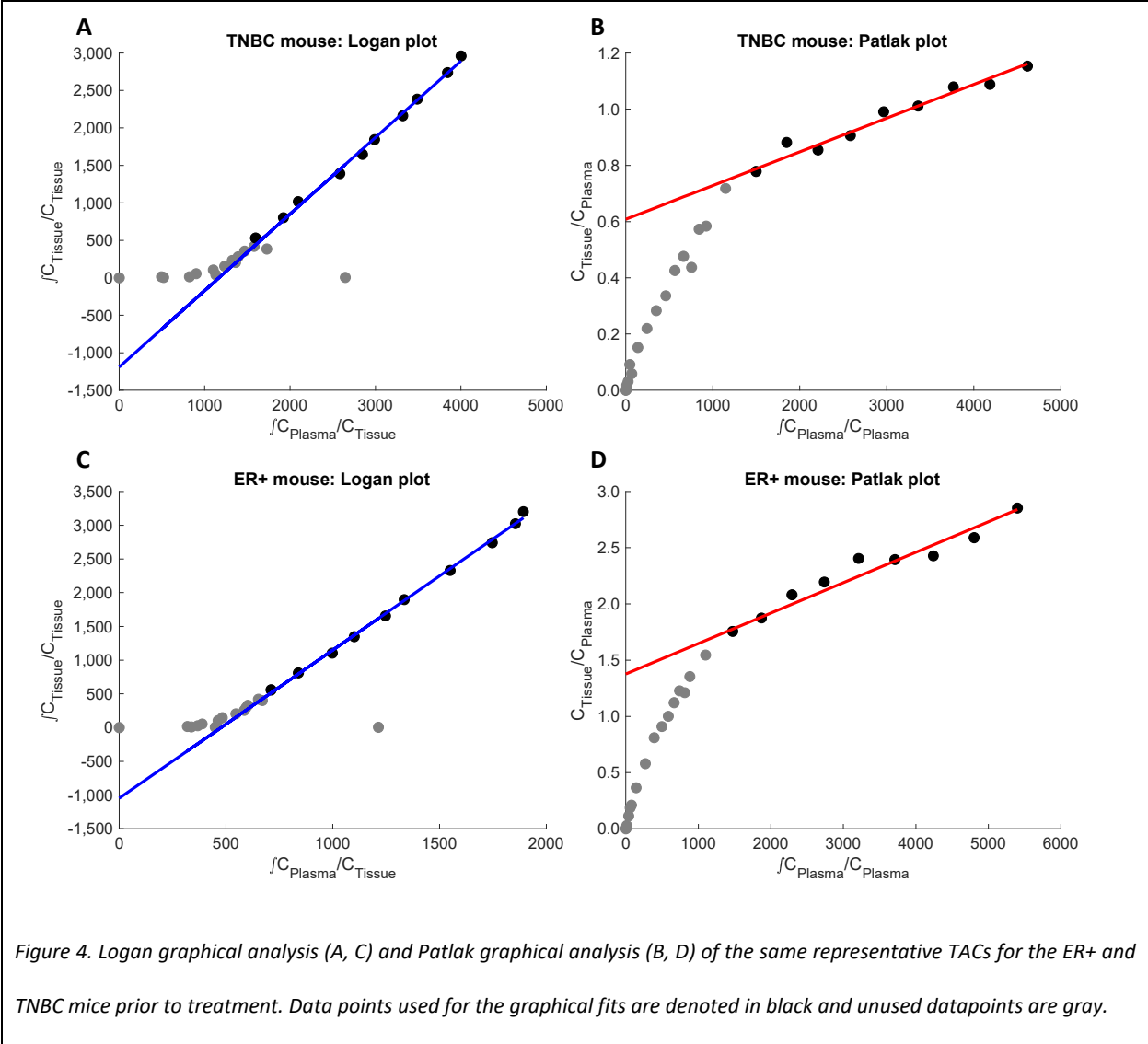


Figure 3. Single-compartment model fit (A, C) and two-compartment model fit (B, D) of the same representative TACs for the ER+ and TNBC mice prior to treatment. The two-compartment fit separately shows the time course of both the reversible (dashed line) and trapped (dash dot line) compartments.



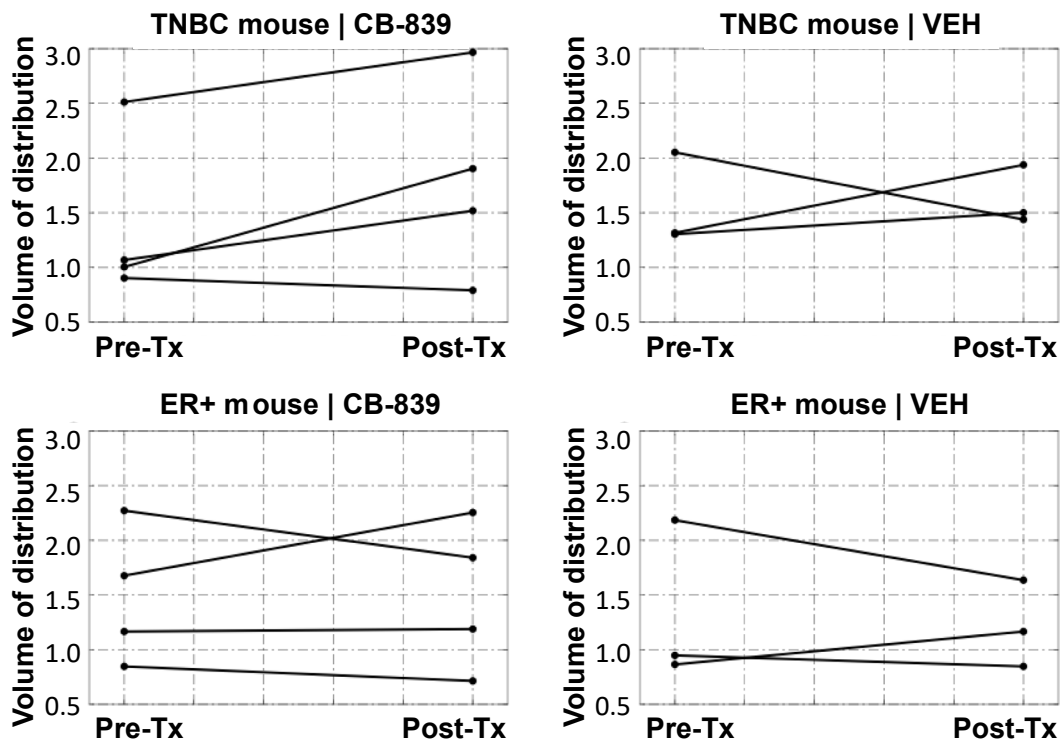


Figure 5. Change in volume of distribution and tumor-to-blood ratio after treatment in tumor xenografts for both TNBC (top) and ER+ (bottom) mice who underwent treatment with a GLS inhibitor (left) or a placebo (right).

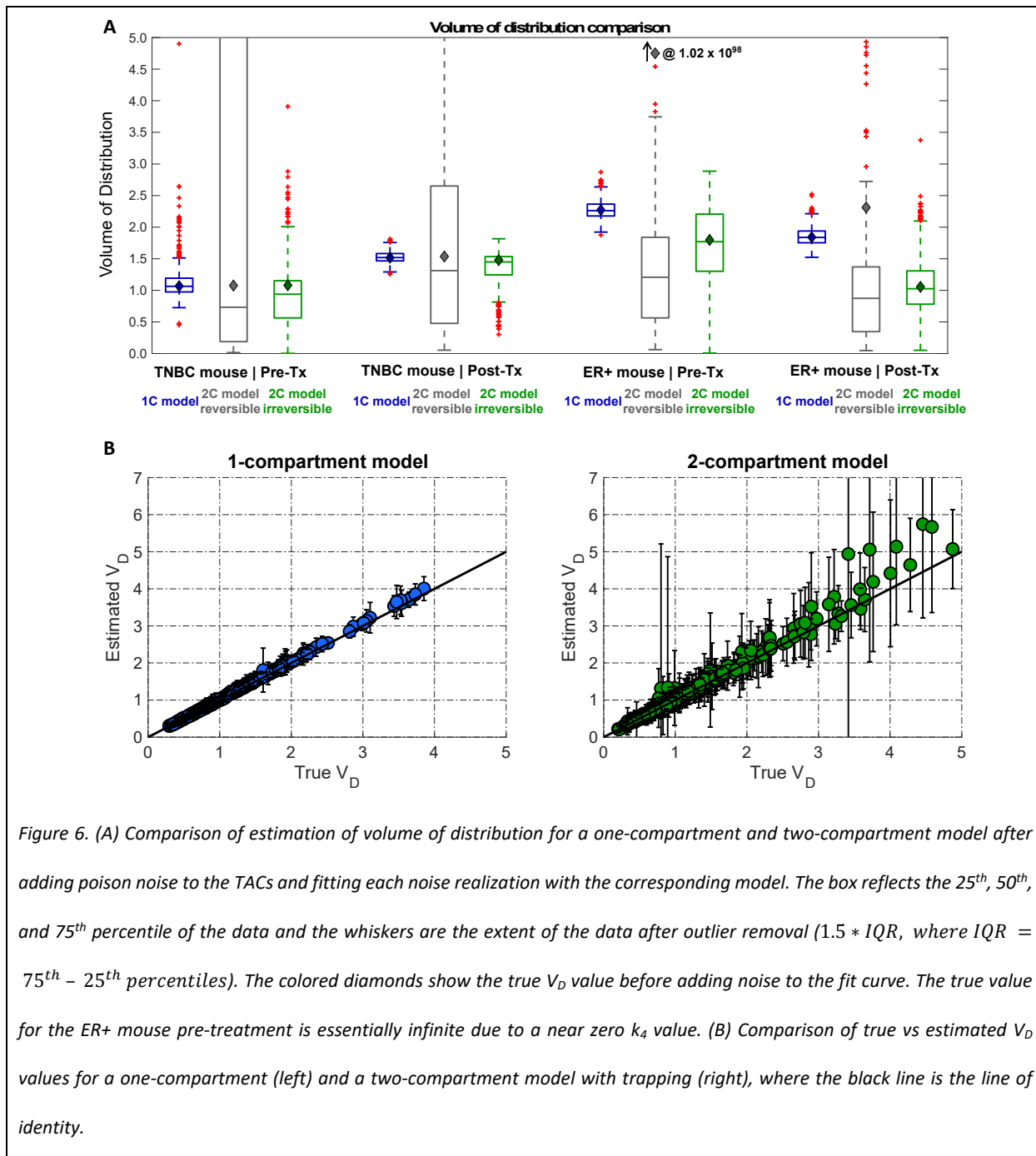


Figure 6. (A) Comparison of estimation of volume of distribution for a one-compartment and two-compartment model after adding poison noise to the TACs and fitting each noise realization with the corresponding model. The box reflects the 25<sup>th</sup>, 50<sup>th</sup>, and 75<sup>th</sup> percentile of the data and the whiskers are the extent of the data after outlier removal ( $1.5 * IQR$ , where  $IQR = 75^{th} - 25^{th}$  percentiles). The colored diamonds show the true  $V_D$  value before adding noise to the fit curve. The true value for the ER+ mouse pre-treatment is essentially infinite due to a near zero  $k_4$  value. (B) Comparison of true vs estimated  $V_D$  values for a one-compartment (left) and a two-compartment model with trapping (right), where the black line is the line of identity.

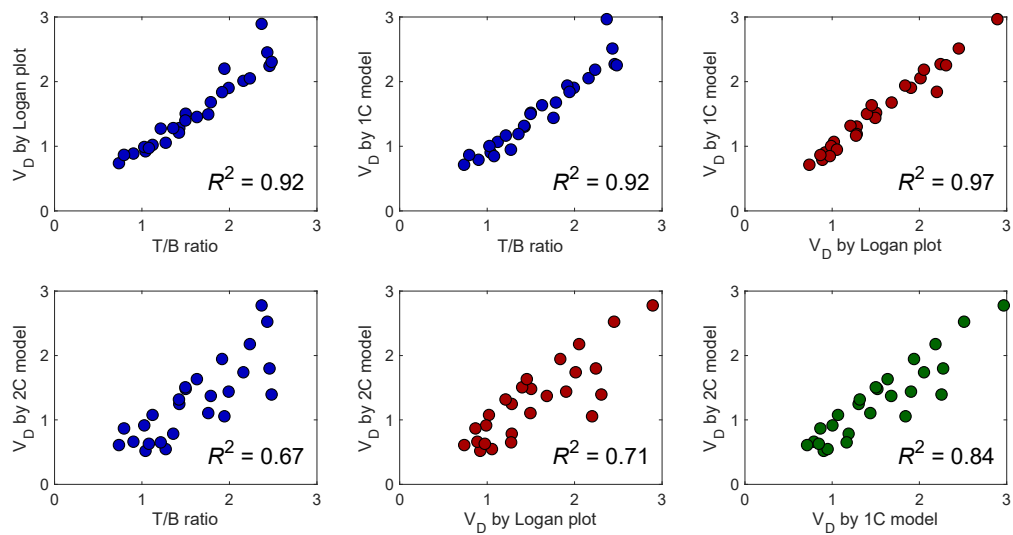
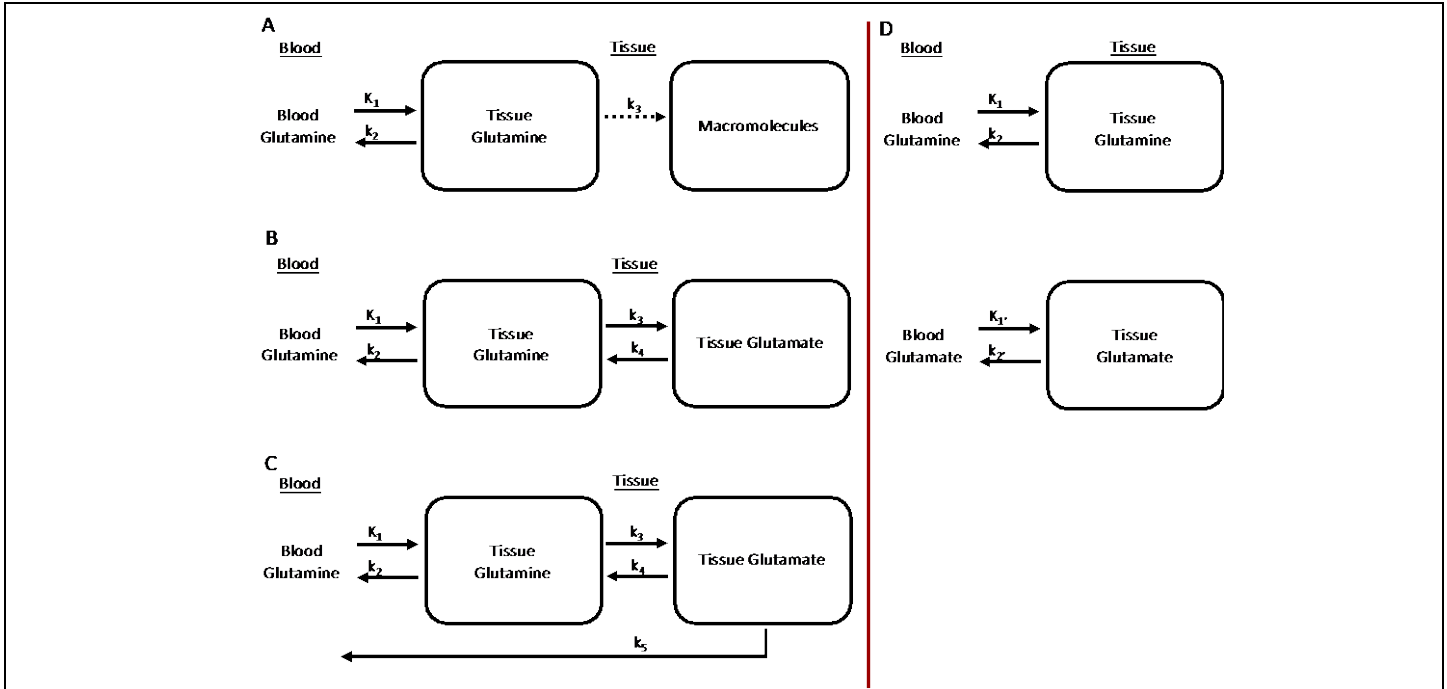


Figure 7. Comparison of volume of distribution of  $^{18}\text{F}$ -Gln by compartmental and graphical analysis, as well as tumor-to-blood ratios.

**SUPPLEMENTAL METHODS**



Supplemental Figure 1. Various proposed models for <sup>18</sup>F-Gln including (A) two-compartment irreversible model with some trapping of <sup>18</sup>F-Gln in macromolecules (same as Figure 1 in Main text), (B) two-compartment reversible model where the second compartment represents tissue glutamate, (C) two-compartment reversible model where the second compartment reflects a glutamate pool, but with efflux from tissue glutamate back to blood, and (D) dual-input two-compartment reversible model including both tissue glutamine and glutamate independently.

**BIAS CALCULATION**

Supplemental Equation 1. Bias and precision calculations for simulations

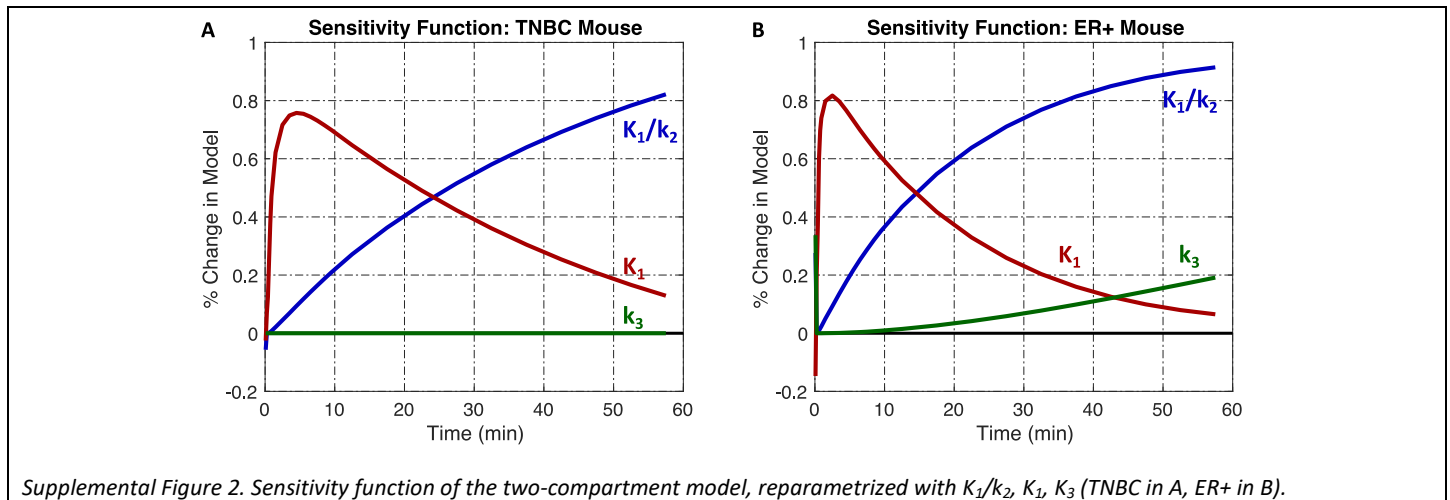
$$bias = 100\% * (x - \hat{x})/\hat{x}$$

$$\%SD = IQR/\hat{x}$$

where  $\hat{x}$  is the true value and  $x$  is the measured value.

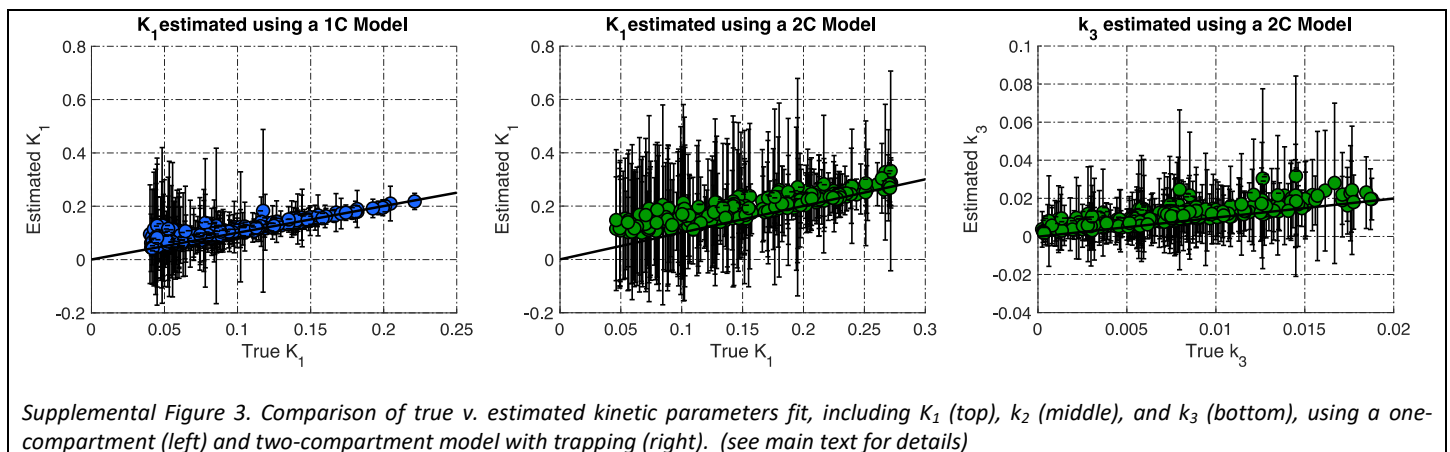
**SUPPLEMENTAL RESULTS**

**MODEL PARAMETERS SENSITIVITY AND IDENTIFIABILITY**

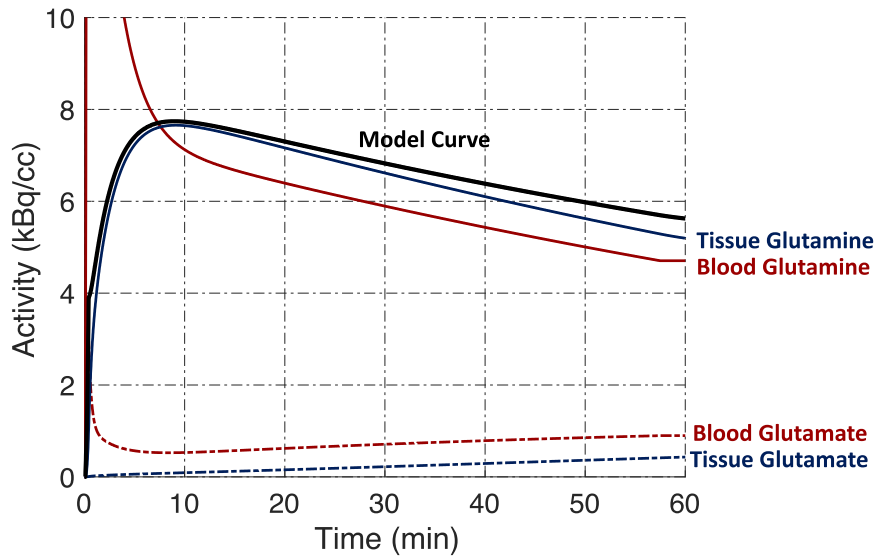


Supplemental Table I. Identifiability matrix of the two-compartment model, reparametrized with  $K_1/k_2$ ,  $K_1$ ,  $K_3$ .

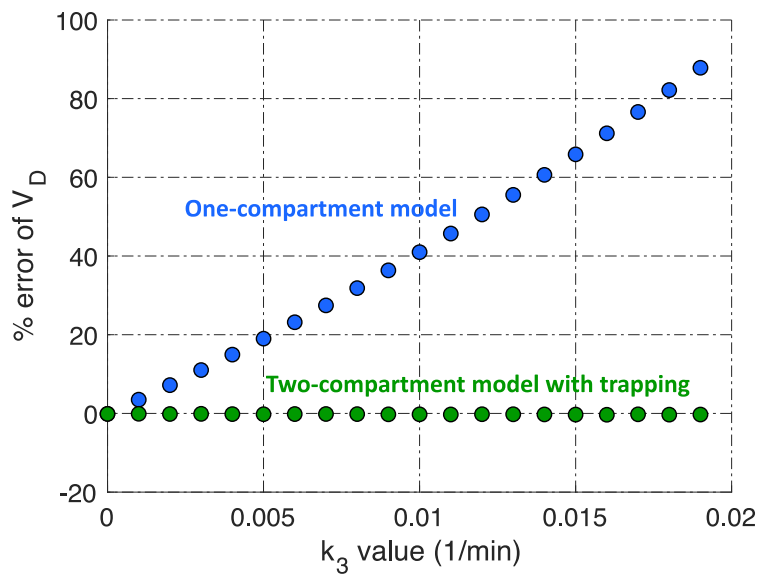
	TNBC				ER+		
	$K_1$	$K_1/k_2$	$k_3$		$K_1$	$K_1/k_2$	$k_3$
$K_1$	1.00	-0.80	0.71	$K_1$	1.00	-0.61	0.14
$K_1/k_2$	-0.80	1.00	-0.97	$K_1/k_2$	-0.61	1.00	-0.70
$k_3$	0.71	-0.97	1.00	$k_3$	0.14	-0.70	1.00



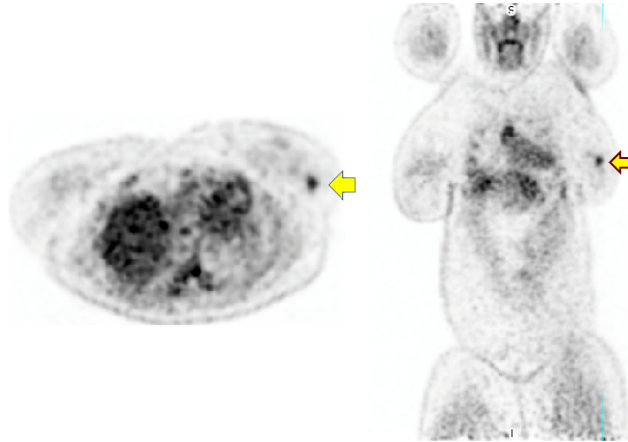
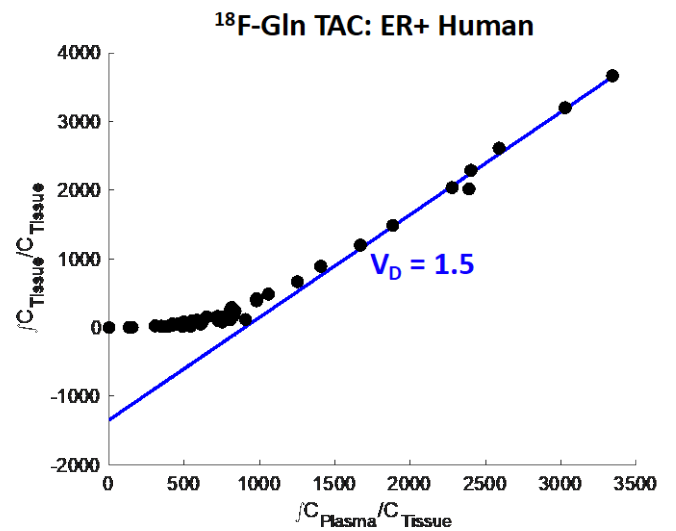
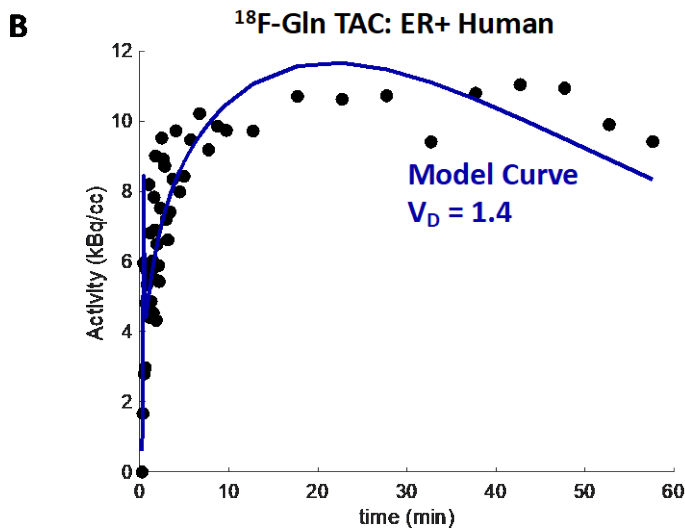
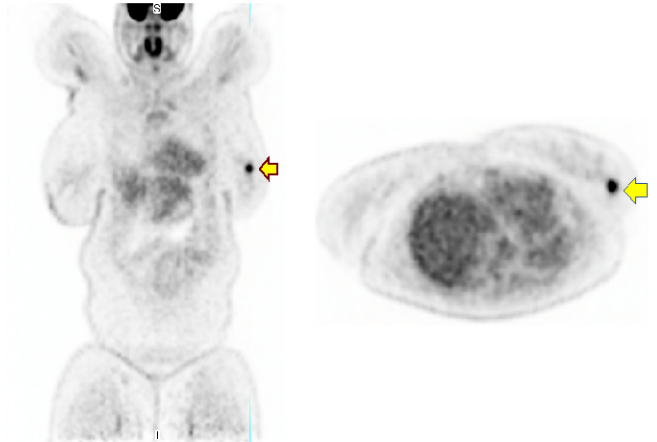




Supplemental Figure 4. TACs for dual-tracer two-compartment reversible model where  $K_1'$  and  $k_2'$  of glutamate is 10% that of glutamine.



Supplemental Figure 5. Error of estimating  $V_D$  using a one-compartment and two-compartment model for  $k_3$  values ranging from  $0 \text{ min}^{-1}$  to  $0.019 \text{ min}^{-1}$ , with  $K_1$  fixed at  $0.138 \text{ ml/cm}^3/\text{min}$  and  $k_2$  fixed at  $0.131 \text{ min}^{-1}$ .

**A**  **$^{18}\text{F}$ -Fluoroglutamine ( $^{18}\text{F}$ -Gln)** **$^{18}\text{F}$ -Fluorodeoxyglucose (FDG)**

Supplemental Figure 6. Preliminary data from human  $^{18}\text{F}$ -Gln study showing (A) axial and coronal image from an ER+ breast cancer patient imaged with  $^{18}\text{F}$ -Gln (left) and FDG (right). The institutional review board approved this study and all subjects signed a written informed consent (Clinical Trial Number NCT03863457). (B) Dynamic  $^{18}\text{F}$ -Gln data fit to a one-compartment model (left) and a Logan plot (right).